ACS OMEGA

Open Access

http://pubs.acs.org/journal/acsodf

Article

Study on the Effect of Structure and Acidity of Hydrocracking Catalyst Support on the Selectivity of Middle Distillate

SongTao Dong,* Ping Yang, and Qinghe Yang

Cite This: *ACS Omega* 2024, 9, 49259−49271

Read Online

ACCESS | Metrics & More | Article Recommendations | Supporting Information

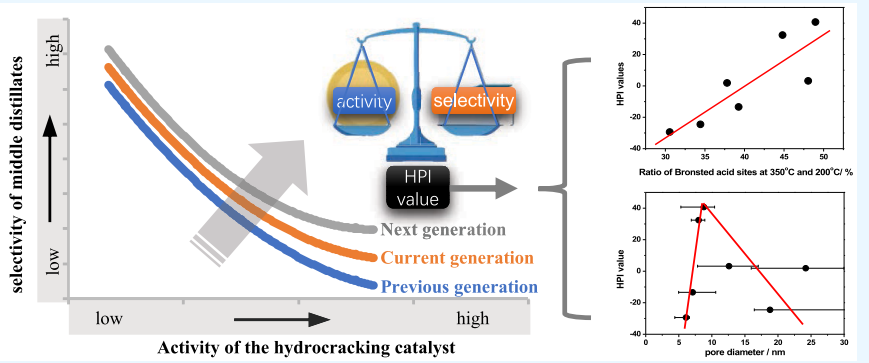

ABSTRACT: Hydrocracking has become the main technology for producing diesel fuel in many refineries, the key process to meeting new product specifications as environmental regulations for transportation fuels become more stringent. The efficacy of the hydrocracking catalyst is a pivotal determinant of the reaction performance. This study leveraged high-throughput experimentation to closely examine the impact of support properties on both the catalytic activity and the selectivity of middle distillates. The findings show that the catalyst's activity is mainly controlled by the amount of Brönsted acid sites and the presence of strong Lewis acid sites within the carrier. An inverse relationship was observed between middle distillate selectivity and catalyst activity, highlighting a trade-off between these two measures of performance. Furthermore, the hydrocracking performance index (HPI), serving as a composite measure of catalyst efficacy, revealed that an optimal pore size and strong Brönsted acidity are important for increasing the HPI value, thereby signifying enhanced catalytic performance. The experimental result matches the bimolecular hydrogen transfer reaction, which is essential in determining the hydrocracking performance index (HPI) value.

1. INTRODUCTION

In the postpandemic era, the global oil market and its demand are projected to rebound, with expectations to revert to prepandemic levels by the close of 2023. The demand for gasoline is anticipated to culminate around 2026,[1] whereas diesel demand is predicted to rebound more swiftly, potentially peaking in the same year. Europe's more forceful objectives and strategies for transitioning to cleaner energy are poised to expedite the phase-out of diesel-powered vehicles in alignment with the "carbon neutrality" target.[2] Concurrently, the deceleration of global economic expansion in the postpandemic period may impose constraints on diesel demand. Nonetheless, aviation fuel is foreseen as a notable driver of oil demand growth in 2022, underscoring the enduring significance of middle distillates, such as diesel and kerosene, as pivotal constituents of the fuel mix in the future.

In the field of hydrocracking catalysts, the key performance indicators are the catalyst activity and the selectivity of middle distillates. Yet, middle distillates serve as an intermediate product in a series of cracking reactions where VGO (vacuum gas oil) is used as the feedstock. There is a trade-off between them: an increase in one often leads to a decrease in the other.[3] It was believed that this challenge can be addressed by carefully tuning the ratio of acidic to hydrogenation sites, which can improve both the activity and the selectivity at the same time.

Given the multitude of factors that impinge upon the performance of hydrocracking catalysts, isolating the influence of a single variable while maintaining all others constant poses a formidable challenge.

The selectivity of hydrocracking catalysts is influenced by a variety of factors, which include the type of acidic components, such as zeolites or amorphous silica−alumina, the choice between single or bimetallic hydrogenation components, the selection and ratio of elements, and the preparation techniques

Received: July 8, 2024
Revised: November 5, 2024
Accepted: November 8, 2024
Published: December 2, 2024

employed. The most significant are the hydrogenation components and the acidic parts of the catalyst as well as the subtle interactions at their active sites. It is hypothesized that a higher hydrogenation activity can lead to a better selectivity for middle distillates. This idea also applies to the performance of different catalytic metals. The characteristics of precious metals like platinum (Pt) and palladium (Pd)[4] are compared with non-precious-metal catalysts such as nickel−tungsten (Ni−W)[5] and nickel−molybdenum (Ni−Mo).[6] Moreover, the ideal amount of these metallic components is an important factor that requires careful evaluation.

In the context of hydrocracking catalysts, the acidic components or supporters exert a defining influence on selectivity, with adsorption and diffusion processes,[7−10] as well as the strategic distribution of acidic centers,[11] emerging as pivotal factors. Amorphous acidic materials have been observed to enhance the selectivity for middle distillates more effectively than molecular sieves,[12] due to their unique structural attributes. Furthermore, the SiO_2−Al_2O_3 composite,[13,14] with its tailored acidity, plays a significant role in modulating catalyst performance.

Molecular sieves characterized by distinctive pore architectures, such as MCM-41,[15] ITQ-21,[16] and MCM-48,[17] play a crucial role in shaping the selectivity of hydrocracking catalysts. Y-type zeolites are particularly important components of these catalysts. Their enhanced features like increased mesoporosity,[18−21] strategically placed acid centers,[22−25] smaller crystallite size,[26−28] and reduced unit cell[29] are key in improving the selectivity for middle distillates.

Moreover, the spatial arrangement of catalytic sites is of vital importance; the closer proximity of hydrogenation and acidic centers facilitates more efficient reactions.[30] Concurrently, optimized reaction conditions, including elevated hydrogen partial pressures,[31] are conducive to enhancing the selectivity of middle distillates. These factors, when harmoniously integrated, offer a synergistic enhancement in the catalytic system's performance.

In conclusion, a multitude of factors collectively dictate the selectivity of the middle distillates in hydrocracking catalysts. Which encompass the type and quantity of metal components, the selection and concentration of molecular zeolites, the formulation of silica−alumina materials, the silica-to-alumina ratio within molecular zeolites, and the methods employed for the modification and treatment of these zeolites. Additionally, the volume of mesoporous pores, the distribution of acid centers across molecular zeolites, and the pore distribution of the support framework are all critical parameters that require meticulous consideration.

Given the numerous variables that influence the selectivity of the middle distillates, it is important to explore the relative importance of each. It is essential to discern which among these factors exerts the most substantial influence, which contributes to a lesser degree, and whether their effects are additive or interactive in nature. Understanding these dynamics is crucial for the rational design and optimization of hydrocracking catalysts that can achieve a balance between activity and selectivity.[3]

In hydrocracking catalysts, a trade-off exists between high activity and selectivity for middle distillates, with one typically increasing as the other decreases—a "seesaw" model. The aim is to optimize catalyst performance by either enhancing both attributes together or boosting one without affecting the other,[32] similar to lifting the seesaw's central pivot.

To assess enhancements in catalyst performance, a new metric was introduced in this article: The hydrocracking performance index (HPI). This index simplifies the evaluation of catalyst efficiency by providing a single measure of the performance balance. In the case of complex catalytic reactions in hydrocracking, the study of factors affecting the selectivity of the middle fraction requires the catalyst to be as simple as possible.

Within the scope of this study, the acidic component of the hydrocracking catalyst was exclusively composed of mesoporous silica−alumina, deliberately free of zeolite additives. To counteract any potential systematic bias that might arise from the preparation of silica−alumina, we employed a variety of preparation techniques were employed. This approach facilitated precise control over the elemental composition of the silica−alumina materials, thereby enabling a more straightforward comparative analysis.

Employing a high-throughput evaluation apparatus, this study explored the factors influencing the selectivity of the middle distillate in the hydrocracking catalysts. By examining seven distinct hydrocracking catalysts, each with unique structural and property profiles, we aimed to achieve a more holistic and precise understanding of the underlying issues. The experimental setup, with its parallel conditions, was meticulously designed to facilitate a robust comparison and evaluation of the catalysts' performance.

2. EXPERIMENTAL SECTION

2.1. Materials. The nitric acid was purchased from Shanghai Aladdin Biochemical Technology Co., Ltd. The pseudoboehmite for catalyst shaping was obtained from Sinopec Catalyst Co., Ltd. Changling division. The mesoporous silica−alumina materials were either homemade or provided by Sinopec Catalyst Co., Ltd. Changling division. The mixed refined VGO was used as feedstock for hydrocracking reactions, which was obtained by adding dimethyl disulfide (DMDS) to the prehydrogenated and refined VGO. The properties of the feedstock are shown in Table 1.

Table 1. Properties of Feedstock Oil

	numerical value	unit	analytic method
density	873.51	kg/m^3	ASTM D1298
sulfur mass fraction	1397.1	g/m^3	ASTM D2622
nitrogen mass fraction	15.8	g/m^3	ASTM D4629
distillation range/%			ASTM D1160
10	292.0	°C	
30	355.9	°C	
50	392.0	°C	
70	424.5	°C	
90	465.6	°C	
95	485.3	°C	

2.2. Preparation of Catalysts. Before the catalyst was prepared, the supports were first prepared. Among the raw materials used. The silica−alumina materials are prepared by three methods:[33] (1) Silica−alumina powders A and C are made by aluminum alkoxide hydrolysis method. Hydrolysis of a solution of mixture of aluminum alkoxide was carried with deionized water, followed by mixing the filtered alumina suspension with a solution of orthosilicic acid. The resulting mixed gels were then spray-dried. (2) Silica-aluminum powders B, D, E, and F are synthesized through the neutralization

https://doi.org/10.1021/acsomega.4c05787
ACS Omega 2024, 9, 49259−49271

precipitation method. A silicon source incorporated to precipitate aluminum hydroxide, followed by aging and drying. (3) Silica-aluminum of powder G is crafted via the sol−gel method, utilizing an aluminum salt in alcohol and orthosilicic acid as sources. It undergoes hydrolysis, condensation, and postgel drying.

A curated selection of seven mesoporous silica−alumina materials, characterized by distinct compositions, acidities, and pore structure properties, was utilized for the preparation of the hydrocracking catalysts. The elemental composition of these materials is detailed in Table 2, providing a comprehensive overview of their chemical constituents.

Table 2. Composition of Mesoporous Silica−Alumina Materials

	composition/%			
silica−alumina materials	Na_2O	Al_2O_3	SiO_2	SO_3
A	/	58.3	41.6	/
B	0.091	71.4	28.0	0.06
C	0.027	62.7	37.1	0.06
D	0.077	62.3	37.3	/
E	0.052	61.4	37.4	/
F	0.084	56.4	41.2	2.11
G	0.012	62.0	37.7	0.21

Upon reviewing the analysis results, it is evident that the compositions of the silica−alumina materials are comparable, with samples A and F exhibiting a SiO_2 content of 41%. Samples C-G contain 37% SiO_2, while sample B displays a lower SiO_2 content of 28%. Across all samples, the mass fraction of Na_2O is notably minimal, being less than 0.1%. These variations are attributed to the synthesis methodologies employed in the preparation of the silica−alumina materials as well as the provenance and purity of the raw materials utilized.

The synthesis of hydrocracking catalysts began with the homogeneous blending and kneading of mesoporous silica−alumina materials, pseudoboehmite, and dilute nitric acid. This mixture underwent extrusion through a precision extruder, yielding cylindrical strips of uniform diameter, precisely 1.6 mm in the outer dimension. The formation of the support structures was completed through a subsequent drying and calcination process.

Following this, the supports underwent impregnation with solutions of nickel nitrate and ammonium metatungstate. The whole process of catalyst synthesis involved a final drying and calcination sequence, which solidified the catalytic components. The resultant catalysts contained an identical composition of 7.0% NiO and 25.0% WO_3 by weight.

To facilitate the systematic study and description, the seven distinct mesoporous silica−alumina materials, selected for their varying acidity and structural properties, were sequentially designated as A-G. Accordingly, the corresponding supports and catalysts were labeled with the prefixes S-A ∼ S-G and C-A ∼ C-G, respectively, ensuring a coherent and orderly reference system throughout the experimental investigation.

2.3. Characterization. The elemental composition of the mesoporous silica−alumina materials was accurately analyzed by utilizing a Shimadzu XRF-1800 X-ray fluorescence spectrometer, ensuring the accurate determination of constituent proportions.

The acidity assessment of the support materials was conducted by employing a NICOLET 6700 Fourier transform infrared (FTIR) spectrometer, with pyridine serving as the probe molecule to quantify acidic sites. The sample preparation involved pressing the materials into wafer forms, followed by a pretreatment regimen at 450 °C under a vacuum of 10^{-3} Pa for a duration of 2 h. This rigorous procedure effectively cleaned the surfaces of the samples. Subsequent to cooling to ambient temperature, pyridine adsorption was carried out for a period of 15 min to attain adsorption equilibrium. The temperature-programmed desorption was executed at 200 and 350 °C under vacuum conditions for each sample. Once the samples reached room temperature, infrared spectra were captured. The quantification of Brönsted and Lewis acid sites within the samples was accomplished by correlating the band intensities observed near 1540 and 1450 cm^{-1}, respectively. The molar extinction coefficients essential for this quantification were referenced from the work of Emeis et al.[34]

Furthermore, the BET (Brunauer−Emmett−Teller) surface area analysis was conducted using a Micromeritics ASAP 2420 analyzer with nitrogen as the adsorbate. The specific surface area, pore volume, and pore size distribution of the materials were ascertained in accordance with the Barrett−Joyner−Halenda (BJH) methodology.

2.4. Catalytic Activity Measurements. The catalytic activity was assessed employing a high-throughput apparatus from HTE, specifically the model X4500.[35] Initially, the catalysts were crushed to a uniform particle size ranging from 16 to 20 mesh. These particles were then loaded into the reaction chamber, followed by the introduction of feedstock oil. The reaction conditions were strictly controlled, with temperatures maintained between 380 and 420 °C to simulate an industrial hydrocracking environment. The hydroprocessing conditions were strictly regulated, with a space velocity set at 1.5 h^{-1} to ensure optimal contact time between the reactants and the catalyst. The hydrogen-to-oil volume ratio was accurately balanced at 900:1 (v/v), and the partial pressure of hydrogen was maintained at 12 MPa. Postreaction analysis was conducted using gas chromatography in accordance with the ASTM D2887 standard, which provided precise determination of the fraction distribution in both the raw materials and the resultant products.

The conversion of raw materials, denoted as X_c, was quantitatively determined through application as follows:

$$X_c = \left(1 - \frac{P_{>350}}{M_{>350}}\right) \times 100\%$$

where $P_{>350}$ is the weight of the component greater than 350 °C in the product and $M_{>350}$ is the weight of the component greater than 350 °C in the raw oil.

The quantification of catalyst activity is denoted by two distinct yet corresponding methodologies. First, the reaction temperature corresponding to a 60% conversion of the feedstock is determined by examining the interplay between temperature and conversion efficiency. Second, the conversion rate of the catalyst at a specified temperature is determined, which subsequently allows for the computation of the reaction rate constant based on the conversion data. The kinetics of the first-order reaction are defined as follows:

$$k = \frac{1}{t} \ln \frac{1}{1 - X_c}$$

https://doi.org/10.1021/acsomega.4c05787
ACS Omega 2024, 9, 49259−49271

Table 3. Pore Structure of Supports

support	surface area/(m^2/g)	pore volume/(mL/g)	R/nm	R_L/nm	R_M/nm	$R_M - R_L$
S-A	403	0.72	7.7	4.6	11.2	6.6
S-B	290	0.77	10.6	7.0	17.8	10.8
S-C	358	0.54	6.1	4.1	6.7	2.6
S-D	272	1.10	24.2	14.5	31.0	16.5
S-E	237	1.11	18.8	16.0	46.5	30.5
S-F	301	0.67	8.8	4.7	10.7	6.0
S-G	334	0.67	8.0	6.7	9.1	2.4

In this equation, k symbolizes the rate constant, X_c denotes the conversion rate and $1/t$ represents the space velocity. It is essential to note that at the designated temperature, the reaction is assumed to follow first-order kinetics.[36,37]

The middle distillate selectivity is expressed as a percentage of the fraction within the temperature range of 132−371 °C relative to the fraction below 371 °C, with the initial amount of the 132−371 °C fraction in the feedstock oil being subtracted. The mass fractions of the components in the specified temperature range for both the product $nP_{132-371}$ and the raw oil $nM_{132-371}$ are taken into account, as well as the mass fractions of the components exceeding 371 °C in the product $nP_{>371}$ and the raw oil $nM_{>371}$. The calculation of the middle distillate selectivity, denoted by X_{MD}, is articulated as follows.

$$X_{MD} = \frac{nP_{132-371} - nM_{132-371}}{nM_{>371} - nP_{>371}}$$

To ensure a standardized comparison of catalyst performance, a uniform feedstock conversion of 60% is applied when calculating selectivity across all catalysts.

The hydrocracking performance index (HPI) is derived through a two-step process. Initially, a linear regression analysis is conducted on the activity (based on reaction temperature corresponding to a 60% conversion) and middle distillate selectivity to establish the regression equation. Subsequently, the deviation of each catalyst's performance point from the regression line is quantified, and this distance is multiplied by 100 to yield the HPI value. A catalyst point positioned above the regression line corresponds to a positive HPI value, indicative of superior performance, while a point below the line is assigned a negative HPI value, reflecting a comparatively lower efficiency.

3. RESULTS AND DISCUSSION

3.1. Properties of Mesoporous Silica−Alumina Materials and Corresponding Supports. The high-temperature calcination process to which the supports are subjected results in the transformation of pseudoboehmite and silica−alumina materials into stable crystalline phases. This conversion ensures that the fundamental structural stability and chemical properties of the catalyst matrix remain unperturbed postmetal loading. Consequently, within the scope of this study, the pore architecture and acidic characteristics of the supports serve as indicative proxies for the intrinsic performance of the catalysts. An examination of Table 3 reveals variations in the specific surface area, pore volume, and dimensional attributes of the pores among the supports.

A detailed analysis of Table 3 highlights visible disparities in the pore size distribution, particularly in the context of the mean pore diameters. Notably, supports exhibiting mean pore diameters beneath the threshold of 10 nm demonstrate a comparatively higher pore concentration. In contrast, those with mean pore diameters exceeding 10 nm are characterized by a relatively diminished pore concentration, indicating a direct correlation between the pore size and concentration that is crucial in the context of catalytic activity and selectivity.

To illustrate the pore distribution of the support, Specifically, the pore diameters at the left and right extremities of the half-peak are designated as the half-high left pore diameter (R_L) and the half-high right pore diameter (R_M), respectively. A minimal difference between the R_L and R_M values indicates a high concentration of pores within the distribution profile.

The locations of several apertures are listed in Figure 1.

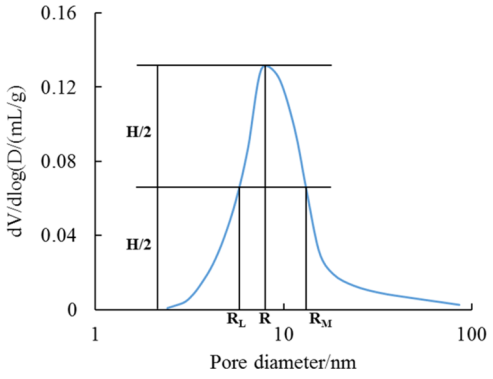

Figure 1. Patterns of pore distribution properties

The pore distribution curve's apex is denoted by the height H, with the half-peak height being H/2. The pore diameter at the curve's zenith is defined as the 'mean pore diameter' (R). Intersections of the pore distribution curve with the half-height level yield two critical pore diameters: the half-height left pore diameter (R_L) on the left side and the half-height right pore diameter (R_M) on the right. The interval between R_L and R_M, known as the pore gap, encompasses most of the pores, thereby providing a representative measure of the pore size distribution.

Detailed characteristics of the support's pore structure are presented in Table 3. The specific surface area of the supports ranges from a maximum of 403 to a minimum of 237 m^2/g, while the pore volume varies from a minimum of 0.54 to a maximum of 1.11 mL/g. A lack of direct correlation between the surface area and pore volume is observed, leading to a diversity in pore diameters among the supports. The pore size R spans from a minimum of 6.1 nm to a maximum of 24.2 nm. To provide a more nuanced description, the values for R_L and R_M are specified, highlighting that pores falling within this range constitute a significant proportion of the total pore volume. The difference between R_M and R_L serves as an indicator of pore concentration, with values ranging from 2.4 to 30.5 nm. Notably, this difference is narrower for supports

https://doi.org/10.1021/acsomega.4c05787
ACS Omega 2024, 9, 49259−49271

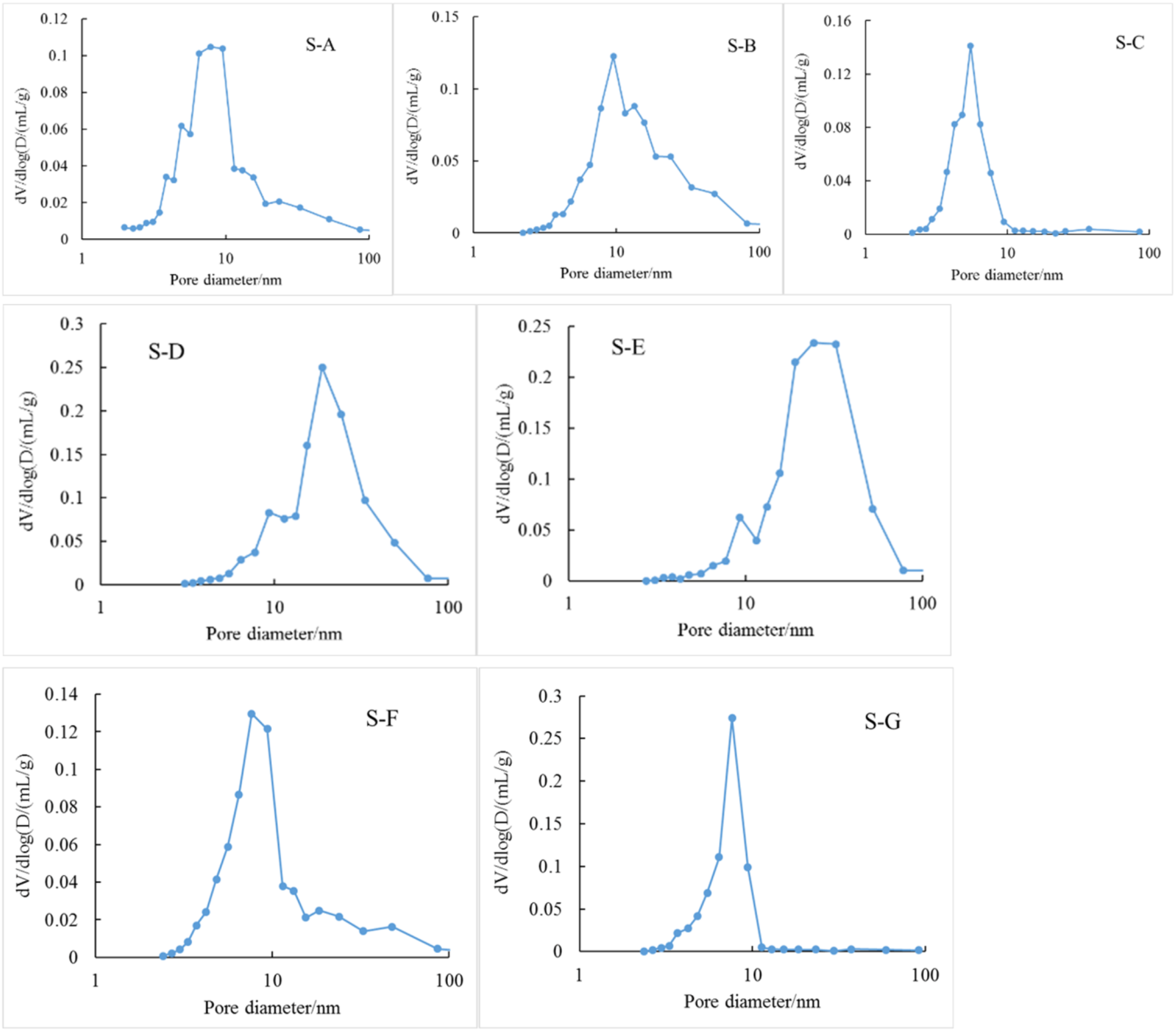

Figure 2. Pore distribution of supports.

with modal pore diameters of 10 nm or less and wider for those with modal pore diameters exceeding 10 nm. Figure 2 illustrates the pore distribution profile of the supports, offering a visual representation of the structural attributes.

The acidity of supports is shown in Table 4. It is generally accepted that the amount of acid measured at the desorption temperature of 200 °C is the total amount of acid, while the amount of acid at 350 °C is the concentration of strong acid. From Table 4, the support acidity, whether Brönsted acid or Lewis acid, has a certain distribution.

Table 4. Acidity of the Supports

	200 °C		350 °C	
support	Brönsted acid (μmol/g)	Lewis acid (μmol/g)	Brönsted acid (μmol/g)	Lewis acid (μmol/g)
S-A	32.6	175.8	12.8	109.0
S-B	15.4	191.7	7.4	98.2
S-C	45.5	233.1	13.9	143.6
S-D	39.5	132.4	13.6	89.7
S-E	41.0	136.8	15.5	93.8
S-F	34.1	181.9	16.7	111.8
S-G	39.5	215.0	17.7	130.0

Examination of the data presented in Table 4 reveals that the carriers C, D, E, and G possess nearly identical silicon oxide contents, with the concentration of Brönsted acid sites at 200 °C falling within a range of 39.5 to 45.5 μmol/g. Similarly, carriers A and F exhibit equivalent silicon oxide levels yet display a slightly lower Brönsted acid concentration at 200 °C, ranging from 32.6 to 34.1 μmol/g. Notably, carrier B presents the lowest silicon oxide content, corresponding to a minimal Brönsted acid amount of merely 15.4 μmol/g at 200 °C. This observation underscores the substantial impact of the silica−alumina material composition on the acidity of the carrier, regardless of the preparation method employed. Intriguingly, a silicon oxide content of approximately 37% correlates with the maximum Brönsted acid concentration at 200 °C; deviations from this level result in reduced acidity. Among materials with similar silicon oxide content, the Brönsted acid concentration at 200 °C follows the order: aluminum alkoxide hydrolysis

https://doi.org/10.1021/acsomega.4c05787
ACS Omega 2024, 9, 49259−49271

method > neutralization precipitation method ≥ sol−gel method. This hierarchy suggests that the preparation technique exerts a discernible influence on the formation of acid centers within the silica−alumina matrix.

Furthermore, the acidity of silica-aluminum materials is significantly lower compared to that of molecular zeolites.[38] This characteristic is advantageous for the enhancement of middle distillate selectivity in hydrocracking catalysts as it ensures compatibility with the metal type and loading requirements.

3.3. Catalyst Activity. To ascertain the catalytic activity of various catalysts, hydrocracking reactions were conducted uniformly at 400 °C. The resulting conversions for the different catalysts are detailed in Table 5, alongside the

Table 5. Conversion of Raw Oil for Each Catalyst at 400°C

catalyst	conversion rate/%	rate constant/(h^{-1})
C-A	66.31	1.632
C-B	32.16	0.582
C-C	76.22	2.154
C-D	57.89	1.297
C-E	63.87	1.527
C-F	67.54	1.688
C-G	76.01	2.141

calculated reaction rate constants (k) derived from the application of a first-order reaction model. Notably, the maximum value of k is observed to be 3.7-fold greater than the minimum, signifying substantial variability in the activity levels among the catalysts examined.

In the realm of hydrocracking catalysts, the cracking reaction is predominantly mediated by acidic centers, with the pore structure of the support typically being a secondary consideration in conversion comparisons. By integrating the acidic properties presented in Table 4 with the catalytic activity data presented in Table 5, several insights emerge:

(1) An analysis comparing catalysts C−E and C−D reveals that the support's Lewis acid content, at both 200 and 350 °C, is similar for each other. However, Catalyst E possesses a higher concentration of Brönsted acid sites than Catalyst D, which corresponds with its higher catalytic activity (E > D). This correlation suggests that Brönsted acid sites significantly contribute to the overall catalytic activity, a trend also observed in the comparison between Catalysts C−A and C−F.

(2) A comparison among Catalysts C−B, C−D, and C−E indicates that while the Lewis acid content of S−B surpasses that of S−E and S−D across the measured temperatures, its Brönsted acid content is approximately half that of S−E. The rate constant for C−B is found to be less than or equal to half that of C−D or C−E, implying a more pronounced impact of Brönsted acid centers on catalytic activity. The specific influence of Lewis acid remains ambiguous.

(3) For Catalysts C−C and C-G, the Lewis acid content at 200 °C is comparable, with a slight excess at 350 °C for S−C. At 200 °C, the Brönsted acid content follows the order S−C > S-G, while at 350 °C, it is S-G > S−C. The activities of C−C and C−G are effectively equivalent, suggesting an equivalence of approximately 6 units of Brönsted acid at 200 °C to 4 units at 350 °C. Furthermore, between C−D and C−G, the Brönsted acid content at 350 °C is 4 μmol/g greater for S−G, aligning with the observed activity trend G > D.

Integrating the above findings, it is evident that Brönsted acid sites are strongly correlated with catalytic activity, whereas the contribution of Lewis acid sites is less distinct. Additionally, the activity is modulated by the varying strengths of the Brönsted acid sites.

To explore the relationship between the support properties and catalyst activity, the correlation coefficients between them were calculated, and the results are shown in Table 6.

Table 6. Correlation between Catalyst Activity and Support Physical Factors

No.	factors	correlation coefficient
1	amount of Brönsted acid sites at 200 °C/(μmol/g)	0.821
2	amount of Lewis acid sites at 200 °C/(μmol/g)	0.442
3	amount of Brönsted acid sites at 350 °C/(μmol/g)	0.773
4	amount of Lewis acid sites at 350 °C/(μmol/g)	0.754
5	ratio of Lewis/Brönsted acid sites at 200 °C	−0.649
6	ratio of Lewis/Brönsted acid sites at 350 °C	−0.450
7	ratio of Brönsted acid sites at 350 and 200 °C	−0.395
8	ratio of Lewis acid sites at 200 and 350 °C	−0.490
9	total amount of Lewis and Brönsted acid sites at 200 °C/(μmol/g)	0.635
10	total amount of Lewis and Brönsted acid sites at 350 °C/(μmol/g)	0.828
11	surface area/(m^2/g)	0.483
12	pore volume/(mL/g)	−0.439
13	mean pore diameter/nm	−0.452

Examination of Table 6 reveals that the correlation coefficients for parameters No. 1, No. 3, No. 4, and No. 10 significantly exceed the threshold of 0.70. This finding underscores that the quantity of Brönsted acid sites at both 200 and 350 °C, alongside the presence of Lewis acid sites and the total acid sites at 350 °C, are principal determinants of catalyst activity. Notably, the pronounced correlation observed for Lewis acid sites at 350 °C with catalytic activity suggests that these dynamic sites may exert a substantial influence on the hydrocracking process.

The negative correlation coefficients associated with parameters No. 5 and No. 6 imply a beneficial effect of an increased presence of Brönsted acid sites coupled with a diminished presence of Lewis acid sites on enhancing catalyst activity. It is noteworthy that a low correlation is detected between the pore structural attributes of the supports (such as surface area, pore volume, and mean pore diameter) and the catalyst's activity. This observation indicates that under the prevailing evaluation conditions, the pore structure is not a pivotal factor in influencing the activity.

Given the substantial correlation identified among catalytic activity and the concentrations of Brönsted acid sites at 200 and 350 °C, as well as Lewis acid sites at 350 °C, a linear regression analysis was conducted to describe their relationship with the rate constant. The analysis proceeded under the assumption that in the absence of acid centers within the hydrocracking reaction, the feedstock would remain unconverted, thereby justifying the simplification of the regression model with an intercept set to zero. The outcomes of this regression analysis are detailed in Table 7.

https://doi.org/10.1021/acsomega.4c05787
ACS Omega 2024, 9, 49259−49271

Table 7. Regression Equation of Support Acidity and Catalyst Activity

	coefficient	standard error	*t*-statistic	*P*-value
intercept distance	0			
amount of Brönsted acid sites at 200 °C	0.023	0.02	1.06	0.35
amount of Brönsted acid sites at 350 °C	0.019	0.06	0.33	0.76
amount of Lewis acid sites at 350 °C	0.0046	0.005	0.91	0.41

	degree of freedom	sum of squares	mean sum of squares	*F*	*p*-value
regression analysis	3	18.6	6.22	59.5	0.0036
residuals	4	0.418	0.10		
total	7	19.1			

Examination of Table 7 reveals that the regression equation's coefficients for 'Amount of Brönsted acid sites at 200 °C' and 'Amount of Brönsted acid sites at 350 °C' are essentially equivalent. However, the coefficient for 'Amount of Lewis acid sites at 350 °C' is notably lower, at approximately one-fifth of the Brönsted acid site coefficients. This difference suggests that despite their strength, Lewis acid sites exert a lesser influence on catalyst activity in comparison to Brönsted acid sites.

Analysis of variance (ANOVA) for the regression equation yielded a *P* value of 0.0036, which is substantially below the threshold of 0.01. This indicates a statistically significant difference and affords us a high level of confidence in the model's validity. Specifically, there is less than a 0.8% risk of erroneously rejecting the null hypothesis, equating to a 99.2% certainty that the null hypothesis—stating no variance among group means—is accurate.

These findings align with the research of Dong Songtao and Zhang Wenmin et al.,[39,40] which posits that both the quantity and strength of acid sites within a catalyst are pivotal in dictating its reactivity.

3.4. Selectivity of Middle Distillate. The efficacy of hydrocracking catalysts is commonly determined by two essential metrics: activity and middle distillate selectivity. These parameters are critical for assessing the catalysts' overall performance in the hydrocracking process. Table 8 presents a compilation of experimental outcomes for seven distinct catalysts, offering a comparative analysis of their activity and selectivity profiles.

In industrial applications, a straightforward and convenient metric is frequently employed to assess the activity of hydrocracking catalysts: the temperature at which the catalyst achieves a 60% conversion. This critical temperature exhibits an inverse relationship with the catalyst's efficacy; higher temperatures are indicative of diminished activity, whereas lower temperatures are suggestive of heightened activity.

Table 8. Activity and Middle Distillate Selectivity of Catalysts

catalyst	activity: reactor temp. for 60% conv./°C	middle distillate selectivity: conv. to 132−371 °C product/%
C-A	393.1	84.0
C-B	421.2	86.7
C-C	388.4	83.5
C-D	397.9	84.6
C-E	394.2	84.0
C-F	392.2	84.5
C-G	389.0	84.1

An analysis of the data presented in Table 8 reveals significant variability in the activity of the evaluated catalysts. The temperature range required for the catalysts to reach the benchmark 60% conversion extends from a minimum of 388 °C to a maximum of 421 °C. Concurrently, the selectivity for the middle distillate fraction demonstrates a range from a low of 83.5% to a high of 86.7%. The relationship between the catalyst activity and the middle distillate selectivity is graphically shown in Figure 3, providing a visual synthesis of the performance metrics.

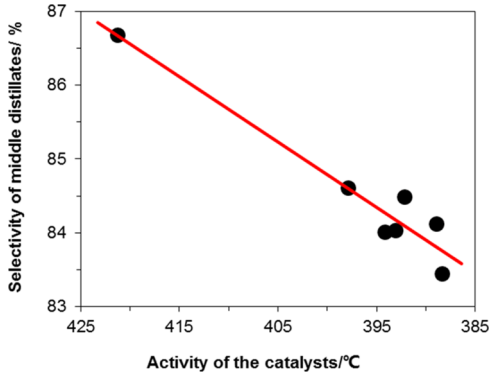

Figure 3. Catalyst Activity and Middle Distillate Selectivity.

The activity of the hydrocracking catalyst and the selectivity of the middle distillate are depicted in Figure 3. A linear regression analysis was conducted on these two variables, and the results are represented by red line. The equation of the linear regression line is shown as follows:

$$y = 0.0883x + 49.455$$

In this equation, y represents the selectivity of the middle distillates and x corresponds to the catalyst activity at a 60% conversion temperature. The coefficient of determination, R^2, is 0.9319, indicating a high degree of correlation between the catalyst activity and selectivity of the middle distillates.

Aligning with the established behavior of classical bifunctional catalysts. This relationship dictates that catalysts exhibiting higher activity, characterized by lower reaction temperatures at a constant conversion, tend to produce lower middle distillate selectivity, and conversely, catalysts with lower activity exhibit higher selectivity.

Among the catalysts evaluated, several comparable levels of performance were demonstrated.

(1) Catalysts A, E, and G, recorded middle distillate selectivity of 84.0%, 84.0%, and 84.1%, respectively, with corresponding activities of 389.0, 393.1, and 394.2 °C. This data suggests a ranking in comprehensive performance of G > A > E, with the activity temperature being directly correlated to the observed performance order. The catalyst supports, as detailed in Tables 3 and 4, exhibit variations in acidity and pore structure, complicating the identification of the key determinants of middle distillate selectivity.

(2) Catalysts F and D displayed closely matched middle fraction selectivity of 84.5 and 84.6%, with activities recorded at 392.2 and 397.9 °C, respectively. The overall

https://doi.org/10.1021/acsomega.4c05787
ACS Omega 2024, 9, 49259−49271

performance comparison favors catalyst for F > D. However, direct comparisons of their acidity and pore structure, which could provide further insight, are not presented.

(3) Catalysts G and C had very similar activity temperatures of 389.0 and 388.4 °C, respectively, and their activities were comparable. The middle distillate selectivity was recorded as 84.1% for G and 83.5% for C, these two catalysts are somewhat comparable, support C, in comparison to G, has a larger pore volume with smaller pore size, a reduced presence of Brönsted acid at 200 °C, and a higher presence of Brönsted acid at 350 °C, alongside a diminished amount of Lewis acid. It is hypothesized that factors such as pore volume, pore size, and the quantities of Brönsted and Lewis acids at both temperatures may exert an influence on selectivity.

The analysis highlights the complexity in attributing middle distillate selectivity to specific factors, as it is challenging to isolate the effects of individual properties when catalysts with identical characteristics vary by only one factor.

3.5. Hydrocracking Catalyst Performance Factors. To compare the reaction evaluation results of hydrocracking catalysts, Dong[35] used the evaluation results of catalysts with different zeolite contents as a benchmark and calculated the distance between the catalyst point and the baseline as a criterion of the performance of this catalyst.

Figure 3 shows that the catalyst performance, measured by activity and selectivity, is directly related to its proximity to the regression line. Points above the line suggest higher selectivity at the same activity or bigger activity at equal selectivity, while points below indicate the opposite. This method enables a comprehensive comparison of catalysts, including those with different activity and selectivity. This study applies the regression line to determine the HPI values for hydrocracking catalysts, as presented in Table 9.

Table 9. HPI Values of Performance Factors of Catalysts

catalyst	HPI value
C-A	−13.4
C-B	3.2
C-C	−29.5
C-D	2.0
C-E	−24.6
C-F	40.9
C-G	32.5

Table 9 presents a clear alignment between the calculated Hydrocracking Performance Index (HPI) values and the previously analyzed comprehensive performance of the catalysts. The sequence of HPI values corroborates the performance order, namely, G > A > E, F > D, and G > C, thereby affirming the reliability of the HPI as a metric. Beyond the results discussed earlier, additional catalysts, not initially covered, have also been evaluated using the HPI, broadening the scope of comparable performance analysis. This novel approach transcends traditional methods by enabling a direct comparison of catalysts with varying activity and selectivity profiles, thereby enriching the depth of catalyst performance evaluation.

The conventional assessment of hydrocracking catalysts is often bothered by the inherent inverse relationship between activity and middle distillate selectivity, complicating the study of catalysts' 'intrinsic' properties. The HPI value, serving as a more holistic and reflective tool of catalyst attributes, avoids this challenge. A pivotal advantage of the HPI is its ability to combine two interrelated performance indicators into a single, unified index, preventing confusion in intense research.

The benchmark comparison facilitated by HPI allows for an assessment of catalyst performance that is decoupled from the individual metrics of activity and middle distillate selectivity. Instead, it focuses solely on the "intrinsic quality" of the catalyst, independent of the quantity of active components and the ratio of hydrogenation to acid centers. This approach is particularly beneficial for an in-depth study of the catalyst's active sites.

Given that all catalysts were prepared with identical types and quantities of active metals following uniform preparation methods and processes, variations in performance can be attributed to the underlying pore structure and acidic characteristics. The utilization of a singular HPI value to summarize the overall performance opens new avenues for exploration. Table 10 elucidates the correlation between the physical and chemical properties of the catalyst supports and their corresponding HPI values, offering further insight into the factors that may influence the catalyst performance.

Table 10. Correlation between HPI Values and Physical Property Factors of Support

No.	factors	correlation coefficient
1	amount of Brönsted acid sites at 200 °C/(μmol/g)	−0.21
2	amount of Lewis acid sites at 200 °C/(μmol/g)	0.14
3	amount of Brönsted acid sites at 350 °C/(μmol/g)	0.44
4	amount of Lewis acid sites at 350 °C/(μmol/g)	0.05
5	ratio of Lewis and Brönsted acid sites at 200 °C	0.14
6	ratio of Lewis and Brönsted acid sites at 350 °C	−0.26
7	ratio of Brönsted acid sites at 350 and 200 °C	0.85
8	ratio of Lewis acid sites at 200 and 350 °C	0.21
9	acid sum of Lewis and Brönsted acid sites at 200 °C/(μmol/g)	0.08
10	acid sum of Lewis and Brönsted acid sites at 350 °C/(μmol/g)	0.12
11	specific surface area/(m^2/g)	−0.17
12	pore volume/(mL/g)	−0.22
13	mean pore sizes/nm	−0.13

An analysis of Table 10 reveals a notable finding: the correlation coefficient for factor No. 7 in relation to the Hydrocracking Performance Index (HPI) values peaks at 0.85, indicating a strong positive association. In contrast, the correlation coefficients for the absolute values of the remaining factors in relation to the HPI values are observed to be consistently below 0.5, suggesting a weaker linkage.

The pronounced correlation between the HPI value and the 'ratio of Brönsted acid sites at 350 °C to those at 200 °C' is particularly significant. It implies that an elevated ratio of single acid sites (Brönsted acid at 350 °C) to the total acid sites (Brönsted acid at 200 °C) within the Brönsted acid centers is beneficial to a higher HPI value. The result suggests that the concentration of strong acid sites is a pivotal factor in enhancing the catalyst's performance. The graphical representation of this relationship, depicting the 'Brönsted acid ratio at 350 and 200 °C' against the HPI value, is elegantly shown in Figure 4.

https://doi.org/10.1021/acsomega.4c05787
ACS Omega 2024, 9, 49259−49271

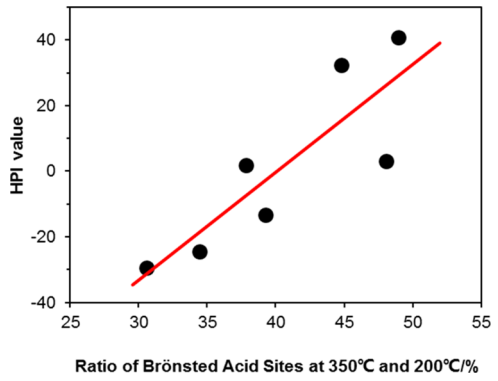

Figure 4. Relationship between the ratio of Brönsted acid sites at 350 and 200 °C and HPI value.

Figure 4 illustrates a significant positive correlation between the proportion of strong Brönsted acids within the total Brönsted acids and the Hydrocracking Performance Index (HPI) value. Within the experimental parameters, an increase in the strong Brönsted acid ratio is directly associated with an elevation in HPI values. This observed correlation is robust and aligns with the calculated correlation coefficients, underscoring the significance of strong acid sites in enhancing catalytic performance. In contrast, other acidic properties exhibited minimal correlation with HPI values, indicating their limited influence on the performance index. An in-depth investigation into the mapping relationships between these acidic properties and HPI values did not yield any substantial correlations or discernible patterns.

According to Table 10, it seems evident that the relationship between the pore structure-related properties and HPI values is inadequate. However, upon further exploration of the correlation between the "mean pore diameter" and HPI values, an unexpected yet modest regularity emerged, as depicted in Figure 5. The figure employs dashed lines to delineate the half-height width range of the support's pore distribution, providing a visual representation of the observed trends.

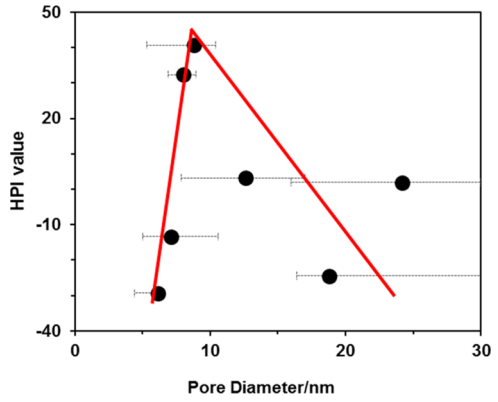

Figure 5. Relationship between the pore diameter and HPI value.

The highest HPI value in Figure 5 is around 10 nm, which is presumably related to the nature of the raw oil used. Except for the "percentage of strong Brönsted acid in total Brönsted acid" and the pore size of the support, no other physical factors were found to be correlated with the HPI values.

Two factors were highly correlated with the HPI values, which in turn were related to the acidity and pore structure of the support, respectively. Considering that the maximum value of the correlation coefficient with the HPI values was 0.85 under a single factor, it is postulated that these two factors may exert mutual influence and interact in a nonlinear manner.

From these findings, a hypothesis was proposed regarding the properties that are likely to enhance HPI values, as detailed below:

(1) The hydrocracking reaction is acid-catalyzed, specifically based on Brönsted acid sites.
(2) An augmentation in acid strength is postulated to be advantageous for the reaction rate.
(3) Pore size is one of the determinant factors in the reaction, with an optimal size range identified; sizes deviating significantly from this range are unfavorable to the reaction efficiency.
(4) The reaction's capacity to terminate the reactivity of small molecule carbenium ions resulting from primary cleavage, thereby mitigating, or preventing secondary cleavage events, is considered beneficial for selectivity and activity.

These hypotheses are formulated to guide future research endeavors aimed at optimizing the catalyst design and performance in hydrocracking processes.

3.6. Discussion. The hydrocracking feedstock is typically VGO with 22−36 carbon atoms, and the middle distillate has 10−22 carbon atoms, which is about half of the feedstock VGO.[41] Therefore, for hydrocracking catalysts, a high primary cracking rate is a guarantee of high activity, while less secondary cracking will result in high middle distillate selectivity. Acidity is an important factor affecting the middle distillate selectivity of hydrocracking catalysts.[42]

The classical hydrocracking reaction mechanism[10] hypothesizes that the feedstock oil molecular undergoes dehydrogenation on the hydrogenation sites of the catalyst, yielding olefins. These olefins subsequently gain a proton from the acidic centers, thereby transforming into carbenium ions. The carbenium-ion mechanism[43] outlines that the primary cracking results in the formation of two types of products: a small olefin molecule and a small carbenium-ion molecule, is depicted as follows.

$$CH_2C^+HCH_2 - CH_2CH_2R' \xleftrightarrow{\text{acid site}} RCH_2CH = CH_2 + C^+H_2CH_2R'$$

Under hydrocracking conditions, the efficiency of small molecule olefins to diffuse to the hydrogenation sites is a critical process. These olefins, upon hydrogenation, are converted into saturated hydrocarbons, which then seamlessly exit the reaction system. This efficient removal is beneficial for preventing the occurrence of secondary cracking reactions. Consequently, an enhancement in the hydrogenation capacity of the catalyst is imperative for enhancing the selectivity of the middle distillates in hydrocracking catalysts.[44] Nonetheless, olefins retain the potential to revert to the formation of carbenium ions on acidic sites, thereby propagating further cracking reactions.

In the present literature on hydrocracking, the fate of primary cracked small molecule carbenium ions has not been extensively explored.[10] However, with their inherent high reactivity, reduction of the reactivity of these carbenium ions is essential to avoid secondary cracking and, in turn, to enhance

https://doi.org/10.1021/acsomega.4c05787
ACS Omega 2024, 9, 49259−49271

the yield of middle distillates. The termination of the reactivity of carbenium ions can be divided into three distinct pathways:

(1) Deprotonation to form an alkene through the removal of a proton.

(2) Formation of an alkane by acquiring a hydride ion, derived from the dissociation of a hydrogen molecule.

(3) Transformation into an alkane via a hydrogen atom transfer from another molecule, facilitated by the exchange of a hydride ion.

These pathways underline the essential role of acid site management in the regulation of the selectivity and activity of hydrocracking catalysts.

3.6.1. Conversion of Carbenium Ion to Olefins by Deprotonation. This reaction is the inverse reaction of olefins forming carbenium ion on the Brönsted acid sites.[40]

$$H_3C - C^+H - CH_2R + X^- \xleftrightarrow{\text{acid site}} H_2C = CHCH_2R + HX$$

In this reaction, the transformation of carbenium ions into olefins is facilitated through a "deprotonation" mechanism, wherein protons are transferred back to the proton-deficient acid sites. Subsequently, these olefins migrate to the hydrogenation sites and upon achieving saturation through hydrogenation are effectively removed from the reaction system.

Empirical simulation data[45] demonstrate that the strength of the acid center significantly modifies acid-catalyzed reactions. It is evident that a rise in the acid strength can markedly reduce the activation energy barrier. However, this increase in acidity also enhances the likelihood of olefins undergoing protonation to regenerate carbenium ions. Consequently, the equilibrium may shift unfavorably to the left, hindering the desired deactivation of carbenium ions and potentially undermining the selectivity of the hydrocracking process.

3.6.2. Conversion of Carbenium Ion to Alkanes by Deprotonation in H_2 Conditions. The reaction is the inverse reaction of alkanes forming carbenium ion at the Brönsted acid sites.[40]

$$H_3C - C^+H - CH_2R + X^- + H_2 \xleftrightarrow{\text{acid site}} H_3C - CH_2CH_2R + HX$$

This reaction proceeds under conditions of high pressure of hydrogen, wherein the consumption of 1 mol of hydrogen results in the concurrent production of a saturated hydrocarbon and a Brönsted acid site.

Dufresne's study findings[31] corroborate the notion that elevating the hydrogen partial pressure exerts a positive influence on the middle distillate selectivity of hydrocracking catalysts. Enhancing the acidity leads to an increased tendency for the formation of carbenium ions, yet paradoxically, it hampers their subsequent deactivation.

For the two reactions mentioned above, while improved acid strength may favor the reverse reactions, it does not align with the objectives of the targeted hydrocracking process. The experimental outcomes do not substantiate these reactions as pivotal pathways for augmenting the hydrocracking performance index (HPI) value. It is conceivable that, within the experimental framework, these reactions may constitute a minor fraction of the overall reaction scheme, thus exerting a limited impact on the catalyst's activity or selectivity.

3.6.3. Hydrogen Transfer Reactions. The reaction to obtain a hydrogen anion from other reactants is a bimolecular hydrogen transfer reaction.[40]

$$R_1^+ + R_2H \xleftrightarrow{\text{acid site}} R_1H + R_2^+$$

In this reaction, the species R_1^+ represents a carbenium ion generated through primary bond cleavage, while R_2H denotes a saturated hydrocarbon. The reaction is thermodynamically favored to proceed to the right if the molecular structure contains a leave-labile hydrogen anion, facilitating a spontaneous reaction progression.[46]

Bimolecular hydrogen transfer reactions have been extensively investigated within the realm of catalytic cracking technology,[47,48] where they are pivotal in enhancing the octane value of gasoline. The selectivity of these hydrogen transfer reactions is commonly quantified by the hydrogen transfer activity (HTA) at low conversion levels,[49] defined as HTA = $R(iC_4)/C(iC_4^=)$. Here, $R(iC_4)$ refers to the rate of isobutane formation, and $C(iC_4^=)$ represents the concentration of isobutene.

Under hydrocracking conditions, olefins in the product mixture are readily hydrogenated, complicating the direct assessment of the extent of hydrogen transfer reaction through conventional catalytic cracking theories.

Sato[50] has reported the occurrence of hydrogen transfer reactions during the hydrocracking of tetralin. Roland and Russell[51,52] have proved the presence of such reactions under hydrocracking conditions. Sayan[53] has conducted a comprehensive study on the reactions involved in hydrocracking, including the intricacies of hydrogen transfer reactions.

For a carbenium ion to be transformed into a saturated hydrocarbon, the acquisition of a hydrogen anion is essential. The conversion of a carbenium ion to a saturated hydrocarbon through hydrogen anion transfer is more likely to occur if the hydrogen anion is readily accessible within the carbenium-ion molecule, and the concentration of potential hydrogen anion donors is sufficiently high.

Under hydrocracking conditions, the feedstock oil's content of saturated hydrocarbons, such as cycloalkanes and chain alkanes, is analyzed in detail.[54] If these saturated hydrocarbons reach a sufficiently high concentration near each acidic center and possess tertiary carbon atoms that are liable to lose hydrogen anions, they can serve as "hydrogen anion reservoirs" reacting with the small molecule carbenium ion from primary cracking for hydrogen anion transfer.

This reaction is expected to yield two significant results:

(1) Small molecule carbenium ions react with hydrogen anions, transforming into saturated hydrocarbons that readily exit the reaction system, thus avoiding secondary cleavage reactions.

(2) Long-chain saturated hydrocarbons, upon losing a hydrogen anion, become large carbenium ions, bypassing the rate-controlling step of carbenium-ion formation in hydrocracking process and thereby significantly enhancing catalyst activity.

For the hydrogen transfer reaction to occur, the presence of both saturated hydrocarbons and carbenium ions is essential, with the small molecule carbenium ion located at the acidic center.

https://doi.org/10.1021/acsomega.4c05787
ACS Omega 2024, 9, 49259−49271

To maximize this reaction, it is essential to 'enrich' a greater amount of bulk saturated hydrocarbons near the acidic center, which undergo cleavage to produce small molecule carbenium ions; the excess hydrocarbons in the neighborhood are fundamental for maximizing the hydrogen transfer reaction. Increasing the acid density is advantageous for enhancing the adsorption of saturated hydrocarbons onto the catalyst surface, elevating the concentration of saturated hydrocarbons near the acidic center, enriching the saturated hydrocarbon molecules, and reducing the average geometric distance between saturated hydrocarbons and small carbenium-ion molecules, thereby further increasing the likelihood of the reaction proceeding. Moreover, higher acid strength is beneficial to promoting the hydrogen transfer reaction.

The pore structure of a catalyst significantly influences its performance, extending beyond the scope of the acidity. As Kobayashi suggested,[55] a catalyst's pore size, when larger than 200 nm, tends to decrease the selectivity for middle distillates. Hadia[56] has also noted a correlation between acidity and pore structure with the selectivity of middle distillates, highlighting the multifaceted role of the catalyst's performance.

The optimal pore size is intricately linked to the characteristics of the feedstock oil.[57] Heavier oils, which possess larger molecular sizes, necessitate larger pore sizes for an effective reaction. The catalyst's pores serve a crucial function as diffusion channels for both reactants and products, with the molecular size of the feedstock oil typically exceeding that of the products. Consequently, the nature of the feedstock oil, particularly its molecular size, exerts the most substantial impact. Heavier feedstock with larger molecular sizes would benefit from larger optimal pore sizes to facilitate the catalytic process.

A pore size that is too small can obstruct the diffusion of macromolecularly saturated hydrocarbons, hindering their enrichment near the acid center. Conversely, an excessively large pore size may result in suboptimal surface coverage. Pore sizes that align with the molecular dimensions of the reactants are more conducive to the concentration of long-chain saturated hydrocarbons near the acid center, which in turn enhances the middle distillate selectivity of the catalyst.

In summary, to maximize the bimolecular hydrogen transfer reaction, a catalyst requires a higher acid strength, increased acid density, and a substantial concentration of long-chain saturated hydrocarbons in the vicinity of the acid center. The bimolecular hydrogen transfer reaction aligns with experimental outcomes and is pivotal in affecting the Hydrocracking Performance Index (HPI) value.

4. CONCLUSIONS

The factors influencing the activity and selectivity of middle distillates of hydrocracking catalysts were investigated utilizing a high-throughput apparatus. It was determined that the quantity of Brönsted acid sites and strong Lewis acid sites significantly influences the hydrocracking activity. Moreover, these distinct acidic characteristics exert varying levels of impact on the activity. To assess the comprehensive performance of a catalyst, the Hydrocracking Performance Index (HPI) was introduced, which integrates both catalytic activity and middle distillate selectivity.

The HPI value is chiefly influenced by two key factors: the ratio of strong Brönsted acid in the total amount of acid sites and the dimensions of the catalyst's pores. An increased proportion of strong Brönsted acid sites relative to the total acid sites, coupled with pore sizes that closely approximate the optimal dimensions for accessibility, results in a higher HPI value. The reaction that is pivotal to the HPI value is associated with a bimolecular hydrogen transfer. The extent to which this reaction occurs is directly proportional to the magnitude of the HPI value, indicating that a more advanced progression of the bimolecular hydrogen transfer reaction leads to an enhanced HPI value.

■ ASSOCIATED CONTENT

Supporting Information

The Supporting Information is available free of charge at https://pubs.acs.org/doi/10.1021/acsomega.4c05787.

Strength of Pearson correlation coefficient (r) value in the literature (Table S1) (PDF)

■ AUTHOR INFORMATION

Corresponding Author

SongTao Dong − *Sinopec Research Institute of Petroleum Processing Co., Ltd, 100083 Beijing, People's Republic of China;* orcid.org/0009-0002-4287-0699; Email: dongst.ripp@sinopec.com

Authors

Ping Yang − *Sinopec Research Institute of Petroleum Processing Co., Ltd, 100083 Beijing, People's Republic of China*

Qinghe Yang − *Sinopec Research Institute of Petroleum Processing Co., Ltd, 100083 Beijing, People's Republic of China*

Complete contact information is available at: https://pubs.acs.org/10.1021/acsomega.4c05787

Notes

The authors declare no competing financial interest.

■ ACKNOWLEDGMENTS

The authors are very grateful to Bao Jun and Zeng Suangqin for providing the silica-aluminum material and acid analysis, and thank Wang Yifan, Li Jian, Zhao Guangle, Zhao Yang, and Mao Yizhao for their work in catalyst evaluation and data analysis. This work was financially supported by research grant from the National Key R&D program of China (No. 202YFA1501204) and China Petrochemical Corporation (Grant No. 123018).

■ REFERENCES

(1) Bing, H.; Chao, Q.; Yong, M. Analysis on the characteristics of China's gasoline consumption market and the trend in the post-pandemic period. *Int. Pet. Econ.* **2023**, *31* (04), 73−78.

(2) Aklilu, A. Z. Gasoline and diesel demand in the EU: Implications for the 2030 emission goal. *Renewable Sustainable Energy Rev.* **2020**, *118*, No. 109530.

(3) Scherzer, J.; Gruia, A. J. *Hydrocracking Science and Technology*, 1st ed.; CRC Press, 1996.

(4) París, R. S.; L'Abbate, M. E.; Liotta, L. F.; Montes, V.; Barrientos, J.; Regali, F.; Aho, A.; Boutonnet, M.; Järås, S. Hydroconversion of paraffinic wax over platinum and palladium catalysts supported on silica−alumina. *Catal. Today* **2016**, *275*, 141−148.

(5) Cui, G.; Wang, J.; Fan, H.; Sun, X.; Jiang, Y.; Wang, S.; Liu, D.; Gui, J. Towards understanding the microstructures and hydrocracking

performance of sulfided Ni−W catalysts: Effect of metal loading. *Fuel Process. Technol.* **2011**, *92* (12), 2320−2327.
(6) Pereyma, V. Y.; Dik, P. P.; Klimov, O. V.; et al. Hydrocracking of vacuum gas oil in the presence of catalysts $NiMo/Al_2O_3$−amorphous aluminosilicates and NiW/Al_2O_3−amorphous aluminosilicates. *Russ. J. Appl. Chem.* **2015**, *88*, 1969−1975.
(7) Weitkamp, J.; Ernst, S. Factors Influencing the Selectivity of Hydrocracking in Zeolites. In *Guidelines for Mastering the Properties of Molecular Zeolites*; Barthomeuf, D.; Derouane, E. G.; Hölderich, W., Eds.; NATO ASI Series, 1990; Vol. *221*.
(8) Benazzi, E.; Leite, L.; Marchal-George, N.; Toulhoat, H.; Raybaud, P. New insights into parameters controlling the selectivity in hydrocracking reactions. *J. Catal.* **2003**, *217* (2), 376−387.
(9) Yan, T. Y. Zeolite-based catalysts for hydrocracking. *Ind. Eng. Chem. Process Des. Dev.* **1983**, *22* (1), 154−160.
(10) Wang, H.; Mao, W.; Wang, K.; Qin, Y.; Li, Q.; Peng, C.; Wang, J.; Sun, Z.; Song, L. Insight into the Effects of Mass Transfer Performance of Y Zeolite on the Product Selectivity of VGO Hydrocracking. *Ind. Eng. Chem. Res.* **2022**, *61* (50), 18270−18281.
(11) Ding, L.; Sitepu, H.; Al-Bogami, S.A.; Yami, D.; Tamimi, M.; Shaik, K.; Sayed, E. Effect of Zeolite-Y Modification on Crude-Oil Direct Hydrocracking. *ACS Omega* **2021**, *6* (43), 28654−28662.
(12) Dik, P. P.; Golubev, I. S.; Kazakov, M. O.; et al. Influence of zeolite content in NiW/Y-ASA-Al_2O_3 catalyst for second stage hydrocracking. *Catal. Today* **2021**, *377*, 50−58.
(13) Hwang, S.; Lee, J.; Park, S.; Park, D.; et al. Production of Middle Distillate Through Hydrocracking of Paraffin Wax over $NiMo/SiO_2$−Al_2O_3 Catalysts: Effect of SiO_2−Al_2O_3 Composition on Acid Property and Catalytic Performance of $NiMo/SiO_2$−Al_2O_3 Catalysts. *Catal. Lett.* **2009**, *129*, 163−169, DOI: 10.1007/s10562-008-9784-y.
(14) Dik, P. P.; Klimov, O. V.; Budukva, S. V.; et al. Silica-alumina based nickel-molybdenum catalysts for vacuum gas oil hydrocracking aimed at a higher diesel fraction yield. *Catal. Ind.* **2014**, *6*, 231−238.
(15) Corma, A.; Martinez, A.; Martinezsoria, V.; Monton, J. B. Hydrocracking of Vacuum Gasoil on the Novel Mesoporous MCM-41 Aluminosilicate Catalyst. *J. Catal.* **1995**, *153* (1), 25−31.
(16) Corma, A.; Díaz-Cabañas, M. J.; López, C.; Martínez, A. Hydrocracking catalysts based on the new large-pore ITQ-21 zeolite for maximizing diesel products. In *Studies in Surface Science and Catalysis*; van Steen, E.; Claeys, M.; Callanan, L. H., Eds.; Elsevier, 2004; Vol. *154, Part C*, pp 2380−2386.
(17) Kenmogne, R.; Finiels, A.; Cammarano, C.; et al. Hydroconversion of n-hexadecane over bifunctional microporous and mesoporous model catalysts. Influence of pore architecture on selectivity. *J. Catal.* **2015**, *329*, 348−354.
(18) Sato, K.; Nishimura, Y.; Honna, K.; et al. Role of HY Zeolite Mesopores in Hydrocracking of Heavy Oils. *J. Catal.* **2001**, *200* (2), 288−297.
(19) Zhang, Xue-Jun.; Wang, Zong-Xian.; Guo, Ai-Jun.; et al. Modification of zeolite Y for preparation of the maxinizing middle distillates hydrocracking catalyst. *J. Fuel Chem. Technol.* **2008**, *36* (05), 606−609. Chinese
(20) Agudelo, J. L.; Hensen, E. J. M.; Giraldo, S. A.; Hoyos, L. J. Effect of USY Zeolite Chemical Treatment with Ammonium Nitrate on Its VGO Hydrocracking Performance. *Energy Fuels* **2016**, *30* (1), 616−625.
(21) Kazakov, M. O.; Nadeina, K. A.; Danilova, I. G.; etal, P. P.; et al. Hydrocracking of vacuum gas oil over NiMo/Y-Al2O3: Effect of mesoporosity introduced by zeolite Y recrystallization. *Catal. Today* **2018**, *305*, 117−125.
(22) Dik, P. P.; Danilova, I. G.; Golubev, I. S.; et al. Hydrocracking of vacuum gas oil over NiMo/zeolite-Al2O3: Influence of zeolite properties. *Fuel* **2019**, *237*, 178−190.
(23) Danilova, I. G.; Dik, P. P.; Sorokina, T. P.; Gabrienko, A. A.; et al. Effect of rare earths on acidity of high-silica ultrastable REY zeolites and catalytic performance of NiMo/REY+Al_2O_3 catalysts in vacuum gas oil hydrocracking. *Microporous Mesoporous Mater.* **2022**, *329*, No. 111547.
(24) Honna, K.; Sato, K.; Araki, Y.et al. HY zeolite-based catalysts for hydrocracking heavy oils. In *Studies in Surface Science and Catalysis*; Delmon, B.; Froment, G. F.; Grange, P., Eds.; Elsevier, 1999; Vol. *127*, pp 427−430.
(25) Agudelo, J. L.; Mezari, B.; Hensen, E. J. M.; et al. On the effect of EDTA treatment on the acidic properties of USY zeolite and its performance in vacuum gas oil hydrocracking. *Appl. Catal., A* **2014**, *488*, 219−230.
(26) Camblor, M. A.; Corma, A.; Martínez, A.; et al. Mild Hydrocracking of Vacuum Gasoil over NiMo-Beta Zeolite Catalysts: The Role of the Location of the NiMo Phases and the Crystallite Size of the Zeolite. *J. Catal.* **1998**, *179* (2), 537−547.
(27) Chen, S.; Yang, Y.; Zhang, K.; Wang, J. BETA zeolite made from mesoporous material and its hydrocracking performance. *Catal. Today* **2006**, *116* (1), 2−5.
(28) Cui, Q.; Zhou, Y.; Wei, Q.; et al. Role of the Zeolite Crystallite Size on Hydrocracking of Vacuum Gas Oil over NiW/Y-ASA Catalysts. *Energy Fuels* **2012**, *26*, 4664−4670.
(29) Ward, J. W. Hydrocracking processes and catalysts. *Fuel Process. Technol.* **1993**, *35*, 55−85.
(30) Kim, M. Y.; Kim, Y.-A.; Jeong, K.-E.; et al. Effect of Al content on hydrocracking of n-paraffin over Pt/SiO_2−Al_2O_3. *Catal. Commun.* **2012**, *26*, 78−82.
(31) Dufresne, P.; Bigeard, P. H.; Billon, A. New developments in hydrocracking: low pressure high-conversion hydrocracking. *Catal. Today* **1987**, *1* (4), 367−384.
(32) Koldachenko, N.; Yoon, A.; Maesen, T.; Torchia, D.; Brossard, D. Hydroprocessing to Maximize Refinery Profitability. In NPRA Annual Meeting, San Diego, CA, 2012, AM-12-41.
(33) Jun, B.; Shuangqin, Z.; Qinghe, Y.; Hong, N.; Xiaofei, Z.; Xiaoyi, S.; Ranran, H. Research progress on preparation and application of amorphous silica-alumina materials. *Pet. Process. Petrochem.* **2024**, *55* (03), 154−161.
(34) Emeis, C. A. Determination of Integrated Molar Extinction coefficients for Infrared Absorption Bands of Pyridine Adsorbed on Solid Acid analysts. *J. Catal.* **1993**, *141* (2), 347−354.
(35) https://www.hte-company.com/fileadmin/content/02Solutions/02TechnologySolutions/01HighThroughputReactorSystems/HighThroughput_Reactor-X-Series-X4500.pdf.
(36) Mohanty, S.; Saraf, D. N.; Kunzru, D. Modeling of a hydrocracking reactor. *Fuel Process. Technol.* **1991**, *29* (1−2), 1−17.
(37) Puron, H.; Arcelus-Arrillaga, P.; Chin, K. K.; et al. Kinetic analysis of vacuum residue hydrocracking in early reaction stages. *Fuel* **2014**, *117*, 408−414.
(38) Sawa, M.; Niwa, M.; Murakami, Y. Relationship between acid amount and framework aluminum content in mordenite. *Zeolites* **1990**, *10* (6), 532−538.
(39) SongTao, D. Study of Hydrocracking Catalyst Selectivity [dissertation]. Beijing. Research Institute of Petroleum Processing; 2001. Chinese.
(40) Zhang, Wenmin.; Smirniotis, Panagiotis G. Effect of Zeolite Structure and Acidity on the Product Selectivity and Reaction Mechanism forn-Octane Hydroisomerization and Hydrocracking. *J. Catal.* **1999**, *182* (2), 400−416.
(41) Rossini, F. D., et al.., *Hydrocarbons from Petroleum*; Van Nostrand Reinhold, New York, 1953.
(42) Lee, J.; Hwang, S.; Seo, J. G.; et al. Production of middle distillate through hydrocracking of paraffin wax over Pd/SiO_2−Al_2O_3 catalysts. *J. Ind. Eng. Chem.* **2010**, *16* (5), 790−794.
(43) Gates, B. C.; Katzer, J. R.; Schuit, G. C. A. *Chemistry of Catalytic Processes*; McGraw-Hill College, 1979; pp 5−25.
(44) Maxwell, I. E. Zeolite catalysis in hydroprocessing technology. *Catal. Today* **1987**, *1* (4), 385−413.
(45) Chen, Dongdong.; Liu, Dongyang.; Wei, Jun.; et al. The effect of acid strength on the mechanism of catalytic pyrolysis reaction of n-hexane in ZSM5: A DFT study. *Appl. Catal., A* **2023**, *665*, No. 119389.

https://doi.org/10.1021/acsomega.4c05787
ACS Omega 2024, 9, 49259−49271

(46) Kazansky, V. B. Adsorbed carbocations as transition states in heterogeneous acid catalyzed transformations of hydrocarbons. *Catal. Today* **1999**, *51* (3−4), 419−434.
(47) Shihuan, W.; Xiang, Z.; Huiping, T. Influences of Hydrogen Transfer Reaction on Catalytic Conversion of Paraffins. *Acta Pet. Sin.* **2016**, *32* (03), 468−476. Chinese
(48) Jianhong, G.; Jun, L.; Youhao, X. Different Reaction Characteristics of Hydride Transfer and Hydrogen Transfer in Catalytic Cracking. *Chin. J. Catal.* **2007**, *1*, 67−72. Chinese
(49) Lukyanov, D. B. A test method for quantitative characterization of zeolite hydrogen transfer activity. *J. Catal.* **1994**, *145* (1), 54−57.
(50) Sato, K.; Iwata, Y.; Yoneda, T.; et al. Hydrocracking of diphenylmethane and tetralin over bifunctional NiW sulfide catalysts supported on three kinds of zeolites. *Catal. Today* **1998**, *45* (1−4), 367−374.
(51) Heck, R. H.; et al. Hydrocracking of n-butane and n-heptane over a sulfided nickel erionite catalyst. *Appl. Catal., A* **1992**, *86* (2), 83−99.
(52) Russell, C. L.; Klein, M. T.; Quann, R. J.; Trewella, J. Catalytic hydrocracking reaction pathways, kinetics, and mechanisms of n-alkylbenzenes. *Energy Fuels* **1994**, *8* (6), 1394−1400.
(53) Sayan, S.; Demirel, B.; Paul, J. Methyldecalin hydrocracking over palladium /zeolite-X. *Fuel* **2000**, *79* (11), 1395−1404.
(54) Zhang, Y.; Zhang, F.; Hu, Z.; et al. Study on changes of hydrocarbons composition of hydrocracking tail oil. *Pet. Process. Petrochem.* **2014**, *45* (11), 44−47. Chinese
(55) Kobayashi, M.; Togawa, S.; Yachi, H.; Ishida, K. Control of macropore structure of hydrocracking catalyst by silica-alumina particle size and influence on hydrocracking activity and middle distillate selectivity. *J. Jpn. Pet. Inst.* **2007**, *50* (5), 278−282.
(56) Hadi, M.; Bozorgzadeh, H. R.; Aghabozorg, H. R.; et al. Effect of acidity and physical properties of nanozeolite catalyst on hydrocracking of vacuum gas oil. *Iran. J. Catal.* **2020**, *10* (2), 111−117.
(57) Sahu, R.; Song, B. J.; Im, J. S.; et al. A review of recent advances in catalytic hydrocracking of heavy residues. *J. Ind. Eng. Chem.* **2015**, *27*, 12−24.

https://doi.org/10.1021/acsomega.4c05787
ACS Omega 2024, 9, 49259−49271